Investigation of particle laden gravity currents using the light attenuation technique

Jean Schneider
Laboratoire d'Energétique et de Mécanique Théorique et Appliquée
Yvan Dossmann (yvan.dossmann@univ-lorraine.fr)
Laboratoire d'Energétique et de Mécanique Théorique et Appliquée
Olivier Farges
Laboratoire d'Energétique et de Mécanique Théorique et Appliquée
Matthieu Régnier
Sébastien Kiesgen de Richter
Laboratoire d'Energétique et de Mécanique Théorique et Appliquée

Research Article

Keywords: gravity currents, light attenuation technique, Kelvin-Helmholtz billows, mixing

Posted Date: August 9th, 2022

DOI: https://doi.org/10.21203/rs.3.rs-1886108/v1

Noname manuscript No.
(will be inserted by the editor)

Investigation of particle laden gravity currents using the light attenuation technique

Schneider J. · Dossmann Y. · Farges O. · Regnier M. · Kiesgen de Richter S.

August 3, 2022 Received: date / Accepted: date

Abstract An extensional use of the light attenuation technique is described to study the dynamics of particle laden flows. The method is validated against an analytical absorption/scattering model. It is then applied to particle laden gravity currents (PLGCs) and provides access to quantitative measurements of the particle mass fraction field. The influence of particle concentration on the turbulent dynamics of the flow and the front velocity are evaluated and discussed. In all experiments heterogeneities in the particle distribution are measured, with the maximum particle concentration in the PLGC front and intermediate particle concentration at the turbulent interface. The results highlight two regimes. In the dilute case, particles have no measurable impact on the turbulent structures observed in the flow nor on the bulk velocity. Particle sedimentation occurs due to mixing between the carrier and surrounding fluids. In the dense case, turbulent structures strongly weaken and the bulk velocity of the PLGC quantitatively decreases as the effective flow viscosity grows.

Keywords gravity currents, light attenuation technique, Kelvin-Helmholtz billows, mixing

1 Introduction

Buoyancy-driven longitudinal currents, known as gravity currents are ubiquitous in environmental flows and also met in industry (Simpson 1982; Sher and Woods 2015). Understanding the dynamics of these flows is a major point of interest for many geophysical phenomenon, such as avalanches, mud flows, dam break, and turbidity currents in the ocean. Particle laden gravity currents (PLGCs) propagate across reservoirs, lakes (Best et al. 2005; Cossu et al. 2015), and oceans (Mulder et al. 2003; Mountjoy et al. 2018). PLGCs are the dominant mechanism for the transport of sediment, nutrients, and pollutants from the continental margin to the deep ocean (Wells and Dorrell 2020).

Lock-release experiments are an usual configuration for the study of turbulent gravity currents (Prastowo et al. 2008; Fragoso et al. 2013; Micard et al. 2016; Hughes and Linden 2016). In this configuration, a lock separates two fluid compartments with different density and composition properties. The horizontal pressure gradient between the two compartements lead to the generation of a gravity current when removing the lock.

In monophasic gravity currents (MGCs), the flow is driven a by a density difference induced by a stratifying agent between two miscible fluids. The two fluids can be of constant density (Shin et al. 2004; Prastowo et al. 2008; Fragoso et al. 2013; Micard et al. 2016; Hughes and Linden 2016) or stratified (Maxworthy et al. 2002; Cortés et al. 2014), which lead to a variety regimes controlled by the Reynolds and Froude numbers. The key role played by mixing effects has been quantified in these laboratory configuration (Prastowo et al. 2008; Fragoso et al. 2013; Micard et al. 2016). The lock-release configuration has been adapted to characterize the flow dynamics including the effects of slope (Odier et al. 2009; Tanimoto et al. 2021) and rotation (Negretti et al. 2021).

In PLGCs, the density difference between the two fluids is induced by the presence of particles that increases the effective density of the flow (Bonnecaze et al.

Laboratoire d'Energétique et de Mécanique Théorique et Appliquée LEMTA - UMR 7563 CNRS-UL - 2 avenue de la Forêt de Haye BP 90161 54505 VANDOEUVRE CEDEX

E-mail: yvan.dossmann@univ-lorraine.fr

1993; Huppert 2006; Sutherland et al. 2018; Wells and Dorrell 2020; Davarpanah Jazi and Wells 2020). In most studies PLGCs have been studied in dilute turbulent regimes or dense laminar regimes (Sutherland et al. 2018; Saha et al. 2013).

A range of techniques are available to understand the dynamics of monophasic gravity currents: shadowgraph ((Prastowo et al. 2008)) Laser Induced Fluorescence (LIF) (Balasubramanian and Zhong 2018), Ultrasound Velocity Profiling (UVP) (Hitomi et al. 2021), Particle Image Velocimetry (PIV) (Krug et al. 2013) and Light Attenuation Technique (LAT) (Fragoso et al. 2013; Micard et al. 2016). However, the experimental studies performed with this technique are limited to MGCs. The investigation of PLGCs remains an experimental challenge. While providing a description of PLGCs dynamics in various concentration, particle properties and stratification regimes, experimental studies carried on PLGCs do not provide a quantitative measure of particle concentration distribution in the flow (Saha et al. 2013; Sutherland et al. 2018; Davarpanah Jazi and Wells 2020). We propose to extend the use of the LAT to investigate the dynamics of the PLGCs at high mass fraction and turbulent regimes. The experimental setup is presented in section 2. The particle induced light attenuation technique and its validation are introduced in section 3. The technique is then applied to investigate the PLGC dynamics relative to the initial mass fraction in section 4, where the local and bulk flow properties are discussed. Conclusions are drawn in section 5.

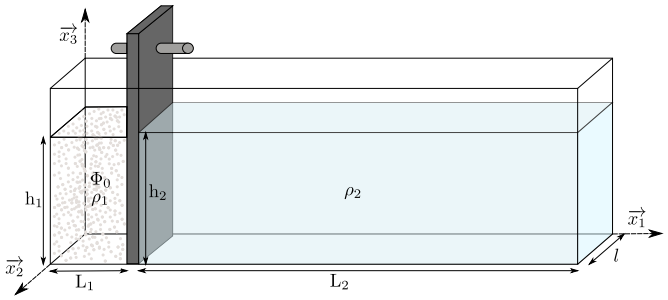

Fig. 1 Sketch of the experimental setup, including the tank, barrier, light panel, particle and camera.

Exp	ρ_1 (kg/m^3)	h_1 (cm)	ρ_2 (kg/m^3)	h_2 (cm)	Φ_0 (%)
Exp A	1039,5	28,5	1015,5	29	0
Exp B	1028,6	27	1004,1	29	3,3
Exp C	1036,5	26,5	1012,5	27	7,1
Exp D	1037,7	28,5	1013,3	29	10,3
Exp E	1035,5	25,5	1010.0	26.2	25.0
Exp F	1034,5	25.1	1010,7	25.2	35.0
Exp G	1035,7	25	1012,5	26	45.0

Table 1 Experimental parameters used for gravity current experiments. The initial density and height of the carrier fluid and the surrounding fluid are (ρ_1, h_1) and (ρ_2, h_2) respectively.

2 Experimental setup and measurement technique

Experiments are conducted in a 150 cm long, 10 cm wide and 35 cm high plexiglas tank. After the tank is filled with freshwater to an height h_1 varying from 24.5 to 29.9 cm, a gate with insulating sides is inserted at $l = 20$ cm from an end of the tank as shown in Fig.1. Salt is dissolved in the lock to reach an homogeneous density ρ_1 in the range $1030 - 1040$ kg.m^{-3}. The particles used are polystyrene spherical beads with a mean diameter $\overline{d} = 0.9$ mm and average density $\rho_p = 1039.5$ kg.m^{-3}. A prescribed mass of particles is poured in a becher filled with saltwater sampled from the lock. The immersed particles are treated in an ultrasonic wave tank for 30 minutes to remove air bubbles. The latter can in fact lead to the formation of particle aggregates floating at the surface. After that time most of the air bubbles are detached from the particles which are poured in the lock. The added particle mass in the lock varied from 0 g to 3000 g corresponding to initial mass fractions ϕ_0 of 0% to 45% in Exp B-G. A particle free experiment (Exp A) is used a reference for the flow dynamics in the Monophasic Gravity Current (MGC) regime. An amount of 5 mL of red food dye is added in the lock as a passive tracer for salinity in Exp A and Exp F. The experimental parameters are listed in Table 1. In all the experiments a typical density difference of $\Delta\rho = 25$ kg.m^{-3} is imposed between the two compartments.

A white LED panel placed behind the tank is used as a quasi-homogeneous light source. Measurements are performed using a 14 bits DSLR Nikon D500 color camera equipped with a Nikkor 53 mm lens. The Nikon camera is also used for to record shadowgraph images in PLGC experiments. The camera is placed at a distance of 350 cm of the tank to limit the effects of parallax. The typical spatial resolution in this configuration is 0.5 mm/pixel. The camera exposure is set to optimize the greyscale level range in the fluid seed with particles. Most measurements are performed with a frame rate of 9 fps.

3 Particle Induced Light Attenuation Technique

3.1 Calibration

The objective of the measurements is to provide high resolution data on the particle and/or stratified flow dynamics in the gravity current. The classical light attenuation technique has been used to infer local, cross-averaged density from light absorption in a dyed fluid (Allgayer and Hunt 1991; Hacker et al. 1996; Sutherland et al. 2012). In the present experiments an extended application of the LAT technique is used to infer cross-averaged local particle volume fractions in PLGGs. The acronym PILAT (Particle Induced Light Attenuation Technique) is adopted in the remainder of the manuscript to refer to the latter technique.

Due to the combined effects of particle scattering and absorption the light issued from the panel is attenuated when traversing the tank. In the calibration step, the light attenuation is calibrated against particle concentration in a shorter tank with the same width as the experimental tank. The calibration tank is filled with water at the same density as the particles. A reference image with an intensity distribution $I_0(x,z)$ is taken before adding particles, with x and z the horizontal and vertical coordinates. A controlled mass of particles is added to the tank before each calibration measurement. The mixture is thoroughly mixed with a hand stirrer before an image with an intensity distribution $I_n(x,z)$ is recorded, where n is the calibration step. The equivalent absorption $A_n(x,z,t) = \log(I_0(x,z)/I_n(x,z))$ is calculated and the integrated added mass m_n is converted into a mass fraction ϕ_n. The calibration is shown in Fig. 2a. A linear increase of absorption analogous to a Beer-Lambert regime is observed for mass fraction up to 3%. For larger mass fractions the absorption increases at a slower but measurable rate up to the packing limit $\phi = 60\%$. The absorption dynamics closely resembles the one of a blue food dye used in previous light attenuation technique experiments (Fig 2b), for which a Beer-Lambert and a saturated regimes are also observed. In particular, the maximum absorption values reached in the calibration for the particle-fluid and the dye are in the same range $A = O(1)$. This shows that the dynamics for measurement of particle mass fraction is potentially as large as the dynamics using dyes in monophasic experiments. The calibration curve is fitted by a spline interpolation function using the Curve Fitting Toolbox in Matlab. The calibration function is then used to convert grayscale fields to mass fraction fields in PLGC experiments.

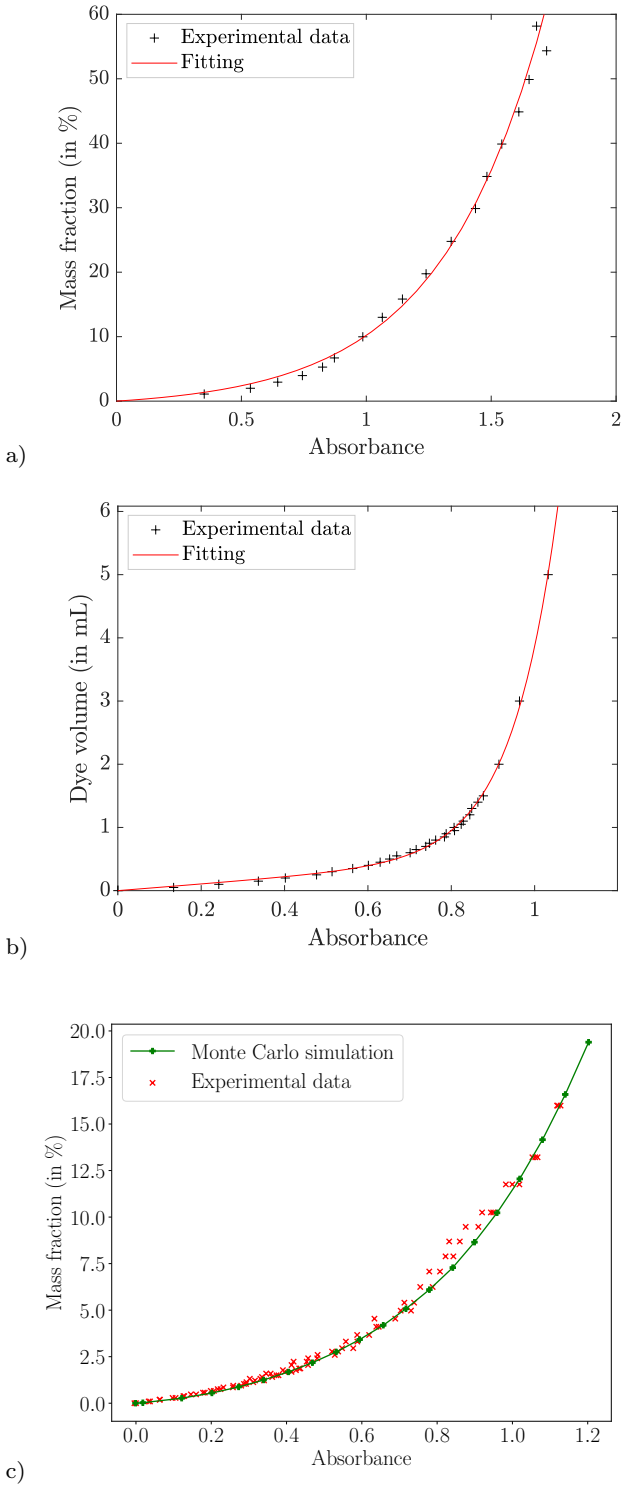

Fig. 2 Evolution as a function of the average light absorbance of: -a) the mass fraction of particles in the suspension relative to the mass of particles added. -b) the volume of dye added. -c) the Monte Carlo model in agreement with the experimental results.

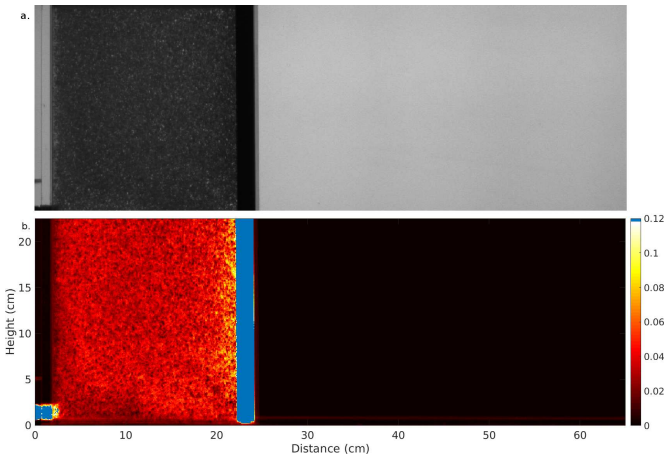

Fig. 3 conversion from grayscale to absorption, using the calibration function. Validation of the absorption to mass conversion in in the left compartment.

An example of conversion from grayscale to mass fraction before the start of an experiment is displayed in Fig.3. The average mass fraction in the left compartment inferred from the added particle mass is 2.95 ± 0.05 %. After the calibration is applied to the grayscale image, one obtains a heterogeneous mass fraction field induced by the particle distribution. The average mass fraction and standard deviation in the left compartment are 3.05 % and 0.62 %. The analyzed average mass fraction matches correctly the inferred value confirming the robustness of the PILAT technique. Note that the barrier affects the light distribution in this picture, as seen by the apparent higher concentrations in the vicinity of the barrier. However the barrier is absent in the course of the experiments which allows for homogeneous background in the experimental field of view.

3.2 Analytical absorption/scattering model

In order to compare the experimental calibration against a theoretical approach, an analytical model based on Monte Carlo method is used. For this purpose, a model of light propagation in the medium is established. It is based on the estimation of the transmittivity $\mathcal{T}$ within the tank by the Monte Carlo method, a reference method in the field of radiative transfers (Howell et al. 2020). The transmitivity is related to the mesured absorption $A = -\log(\mathcal{T})$ as $\mathcal{T} = I(x,z)/I_0(x,z)$.

In the studied case, the medium is considered as a participating medium with heterogeneous radiative properties and the light source emits Lambertian radiation. In order to represent as accurately as possible the heterogeneities of the medium, we use a null-collision Monte Carlo algorithm (Galtier et al. 2013) whose extinction coefficient is presented in the eq.5. The representations of the interactions between matter and radiation are all probabilised : the Beer-Lambert law is simply an expression of the probability of photons travelling a given distance before being absorbed or scattered while the Henyey-Greensein phase function corresponds to the probabilities that a photon initially in a $\mathbf{u_j}$ direction will scatter or be reflected in a direction $\mathbf{u_{j+1}}$ and the nature of the medium is defined as a propensity depending on the volume fraction.

The transmitivity expression is then expressed in an iterative form as presented in the equations eq.1 and eq.2. The scattering phenomena are represented by a Henyey-Greenstein phase function (eq.4) whose asymmetry factor value $\mathbf{g} = 0.92$ comes from the work of Shahin et al. (2019). The absorption/scattering optical path stops when absorbed by water or polystyrene. In order to identify the absorption and scattering coefficients of the polystyrene used in the experiment, the transmitivity estimation model is combined with a particle swarm optimisation (PSO) code (Eberhart and Kennedy 1995). This results in a very good agreement between the experimental measurements and the absorption/scattering model as shown in Fig 2c.

4 Gravity current dynamics

4.1 Quasi-inertial regime ($\Phi_0 < 10\%$)

The reference experiment A shows the development of a monophasic gravity current with turbulent features commonly observed in lock-release experiments (Fig. 4). The current front where large density and velocity gradients, along with a weak mixing occur precedes the head region. In the latter the formation of Kelvin-Helmholtz billows and shear instabilities contribute to an intense mixing between the carrier and the surrounding fluids. Mixing processes weaken in the body and tail regions of the gravity current, as extensively described in (Balasubramanian and Zhong 2018).

PLGCs with low initial mass fractions are displayed in Fig. 5 (exp B, $\Phi_m = 3.3\%$), 6 (exp C, $\Phi_m = 7.1\%$), 7 (exp D, $\Phi_m = 10.3\%$).

When opening the gate, the development of a turbulent gravity current similar to exp A is observed in exp B, C, D. The front exhibits a similar shape and vortices associated with Kelvin-Helmoltz billows are observed in all experiments. The periodicity of the billows is clearly identified as shown on Fig. 6 d.

Important horizontal and vertical gradients in the particle distribution in the gravity current are measured in exps C and D. The largest concentrations are located near the current front where mixing is limited, while they are weaker in the interfacial region.

$$\mathcal{T}(\mathbf{x_0},\mathbf{u_0},l_0)=\int_{\mathcal{S}_{in}}\mathrm{d}\mathbf{x_0}\int_0^{2\pi}\mathrm{d}\mathbf{u_0}\int_0^{+\infty}\mathrm{d}l_0\,p_{X_0}(\mathbf{x_0})p_{U_0}(\mathbf{u_0})p_{L_0}(l_0)$$
$$\times\begin{cases}\mathcal{H}(l_0<l_{out}(\mathbf{x_0},\mathbf{u_0})\times\begin{cases}\mathcal{H}(r_0<\%v)\times\begin{cases}\mathcal{H}\left(r_1<\dfrac{k_{a,p}}{\hat{k}}\right)\times 0\\ +\mathcal{H}\left(r_1<\dfrac{k_{a,p}+k_{s,p}}{\hat{k}}\right)\displaystyle\int_{4\pi}\phi(\mathbf{x_1},\mathbf{u_0}|\mathbf{u_1},\mathbf{g})\times\mathcal{T}(\mathbf{x_1},\mathbf{u_1},l_1)\end{cases}\\ \mathcal{H}(r_0>\%v)\times\begin{cases}\mathcal{H}\left(r_1<\dfrac{k_{a,w}}{\hat{k}}\right)\times 0\\ +\mathcal{H}\left(r_1>\dfrac{k_{a,w}}{\hat{k}}\right)\times\mathcal{T}(\mathbf{x_1},\mathbf{u_1}=\mathbf{u_0},l_1)\end{cases}\end{cases}\\ \mathcal{H}(l_0>l_{out}(\mathbf{x_0},\mathbf{u_0})\times 1\end{cases}\tag{1}$$

$$\mathcal{T}(\mathbf{x_j},\mathbf{u_j},l_j)=\int_0^{+\infty}\mathrm{d}l_j\,p_{L_j}(l_j)$$
$$\times\begin{cases}\mathcal{H}(l_j<l_{out}(\mathbf{x_j},\mathbf{u_j})\times\begin{cases}\mathcal{H}(r_0<\%v)\times\begin{cases}\mathcal{H}\left(r_1<\dfrac{k_{a,p}}{\hat{k}}\right)\times 0\\ +\mathcal{H}\left(r_1<\dfrac{k_{a,p}+k_{s,p}}{\hat{k}}\right)\displaystyle\int_{4\pi}\phi(\mathbf{x_{j+1}},\mathbf{u_{j+1}}|\mathbf{u_j},\mathbf{g})\times\mathcal{T}(\mathbf{x_{j+1}},\mathbf{u_{j+1}},l_{j+1})\end{cases}\\ \mathcal{H}(r_0>\%v)\times\begin{cases}\mathcal{H}\left(r_1<\dfrac{k_{a,w}}{\hat{k}}\right)\times 0\\ +\mathcal{H}\left(r_1>\dfrac{k_{a,w}}{\hat{k}}\right)\times\mathcal{T}(\mathbf{x_{j+1}},\mathbf{u_{j+1}}=\mathbf{u_j},l_{j+1})\end{cases}\end{cases}\\ \mathcal{H}(l_j>l_{out}(\mathbf{x_j},\mathbf{u_j})\times 1\end{cases}\tag{2}$$

$$p_{L_j}(l_j)=\hat{k}(\mathbf{x_j}+l_j\mathbf{u_j})\exp\left(-\int_0^{l_j}\hat{k}(\mathbf{x_j}+l'_j\mathbf{u_j})\,\mathrm{d}l'_j\right)\tag{3}$$

$$\phi(\mathbf{x_{j+1}},\mathbf{u_{j+1}}|\mathbf{u_j},\mathbf{g})=\frac{1}{4\pi}\frac{1-\mathbf{g}(\mathbf{x_{j+1}})^2}{(1+\mathbf{g}(\mathbf{x_{j+1}})^2-2\mathbf{g}(\mathbf{x_{j+1}})\cos(\theta))^{3/2}}\tag{4}$$

$$\hat{k}=\max\left(k_{a,w},k_{a,p}\right)+k_{s,p}\tag{5}$$

$$\mathbf{x_j}=\mathbf{x_{j-1}}+l_{j-1}\mathbf{u_{j-1}}\tag{6}$$

The progressive particle sedimentation can be explained by mixing effects between the carrier and surrounding fluids. In fact, as the current advances, diapycnal mixing contributes to a gradual decrease of the density of the carrier fluid that become less dense than neighbouring particles. Hence, buoyancy forces are no longer able to sustain particles, which result in their sedimentation. This phenomenon leads in particular to a large increase in the particle concentration up to a factor of three in the current front with respect to the upper mixing region as can be seen in Fig. 6e and 7e.

This sedimentation process also occurs in exp B, although less visible as mass fraction measurements are limited in the interfacial region due to low particle concentration (Fig. 5**(d)**).

After reflection on the right end wall, the gravity current propagates rightwards. Turbulent structures in the MGC have weakened in the course of the propagation and interaction with the end wall, which results in a decrease of the maximum current height, from $O(15$ cm) to $O(10$ cm). In the PLGC case instead a dramatic collapse of the particle flow is observed in Fig. 5**(f)** 6**(f)** 7**(f)**, with a particle current maximum height decreasing to $O(5$ cm). The collapse leads to an increase of the particle concentration with mass fractions reaching values larger than 20% in most of the gravity current below the interface.

4.2 Non-newtonian regime ($\Phi_0 > 20\%$)

For increasing mass fraction Φ_0, effects of particle-particle interactions lead to an increase of the effective viscosity of the flow. As a result, turbulent structures at the interface progressively weaken from Exp E (not shown), to Exp F then G.

Experiment F has been performed by adding a red dye as a tracer of the carrier fluid. The dye fluorescence properties allow to carry out PILAT and density measurements (after calibration) with a single camera.

As in the case of the inertial regime, the front, head, body and tail of the PLGC are observed in Exp F (Fig. 8 **(c)**).

In the initial course of the current propagation, one observes that the carrier fluid hardly separates from the particles in the front and at the interface between the

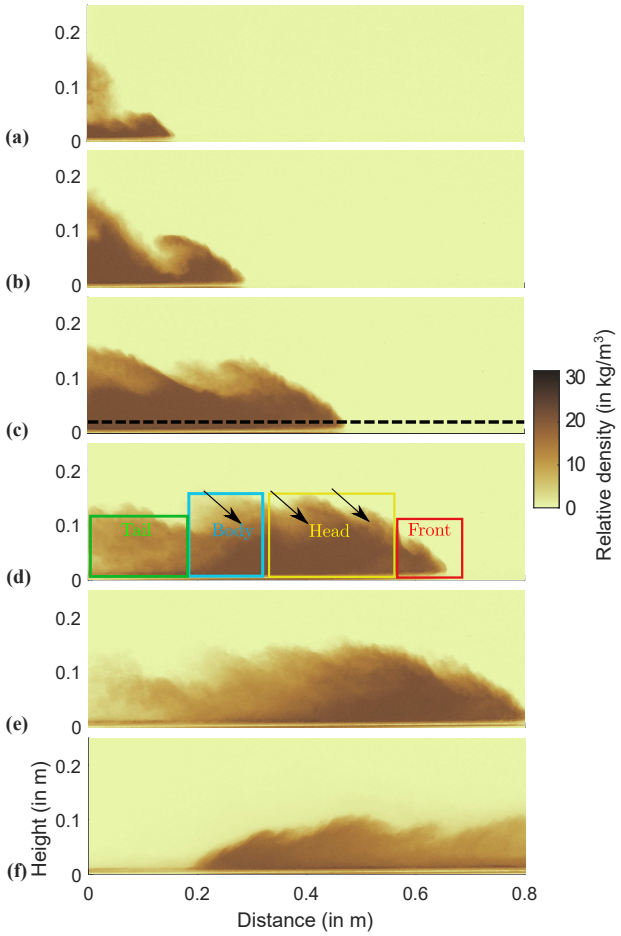

Fig. 4 Figure of a MGC experiment with an initial density difference between the 2 compartments of $\Delta\rho = 24$ kg.m^{-3} . These figures were obtained from photos taken (a) 4.25s, (b) 5.75s, (c) 7.25s, (d) 9.75s (e) 11.25s, (f) 33.25s after opening the gate.

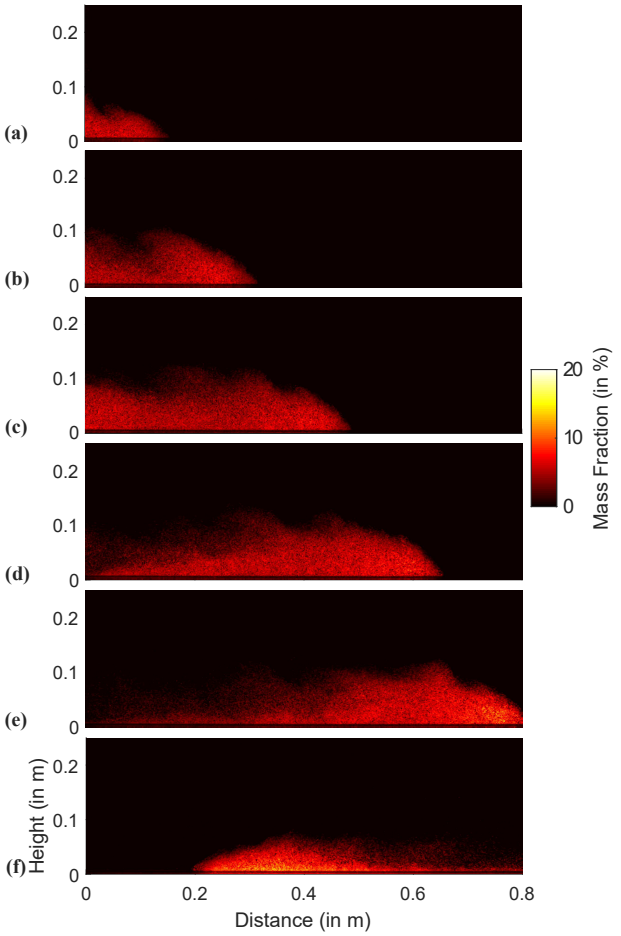

Fig. 5 Figure of a PLGC experiment with an initial density difference between the 2 compartments of $\Delta\rho = 24.5$ kg.m^{-3} and an initial mass fraction of $\Phi_m = 3.28\%$. These figures were obtained from photos taken (a) 4.25s, (b) 5.75s, (c) 7.25s, (d) 9.75s (e) 11.25s, (f) 33.25s after opening the gate.

body and the surrounding fluid, as illustrated in Fig. 8 **(c)**. It is only due to breaking of the K-H billows in the current tail that flow separation is initiated (Fig.8 **(d)**). It is further enhanced in the course of the current propagation and in the return flow that occur in an already stratified environment. 8 **(e)**. In the final stage of the experiment, the dense particle region is much thinner than the dense fluid layer.

In the Experiment G the current height has greatly decreased compared to the inertial regime. While billows are still visible up to heights greater than 15 cm in Exp A-D, the development of such billows are strongly limited in Exp G (instabilities are still visible in Fig. 9**(d)**) and the maximum current height is $O(10)$ cm.

4.3 Particle influence on the front velocity

The front velocity is a bulk property that enables to characterize the overall impact of the particles on the PLGC dynamics. The impact of Φ_0 on the gravity current velocity is analyzed here through the temporal evolution of the front position shown in Fig. 10.

Subsequently the nondimensional velocity is plotted against the relative lock viscosity assessed from the Einstein's relation for viscosity $\eta_r = (1 - \phi/\phi_M)^{-2}$, with ϕ_M the volume fraction at close packing as shown in Fig. 11 a and b.

The velocity during the first transit for the four experiments in the quasi-inertial regime has a typical value of $0,13$m.s^{-1}, in agreement with the analytical value predicted by Simpson (1982) $u = \frac{1}{2}.\sqrt{g'.H} = 0,132$ m.s^{-1}. No significant difference is observed between the MGC and PLGC. The particle effect on the

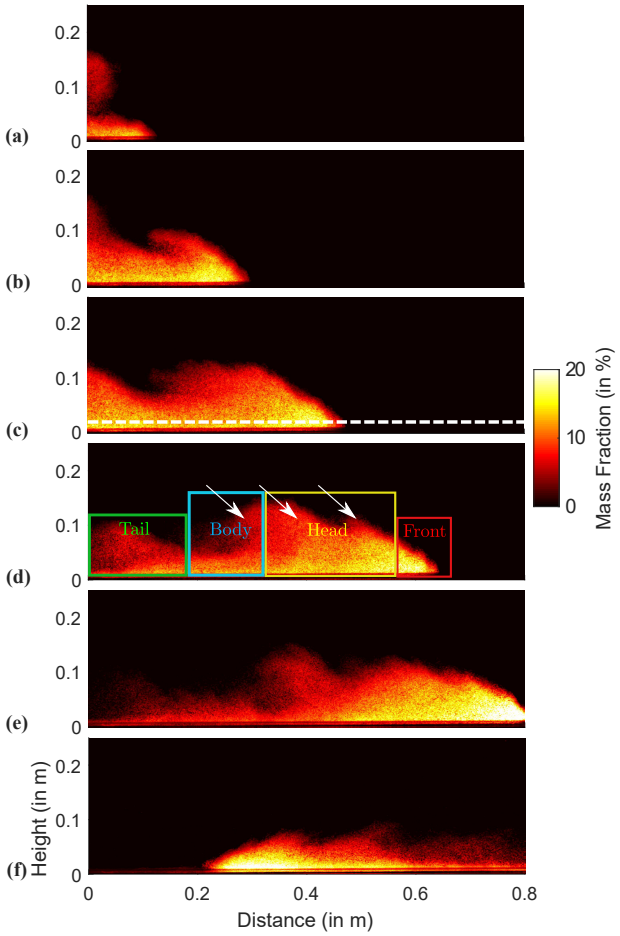

Fig. 6 Figure of a PLGC experiment with an initial density difference between the 2 compartments of $\Delta\rho = 24$ kg.m^{-3} and an initial mass fraction of $\Phi_m = 7.14\%$. These figures were obtained from photos taken (a) 4.25s, (b) 5.75s, (c) 7.25s, (d) 9.75s (e) 11.25s, (f) 33.25s after opening the gate.

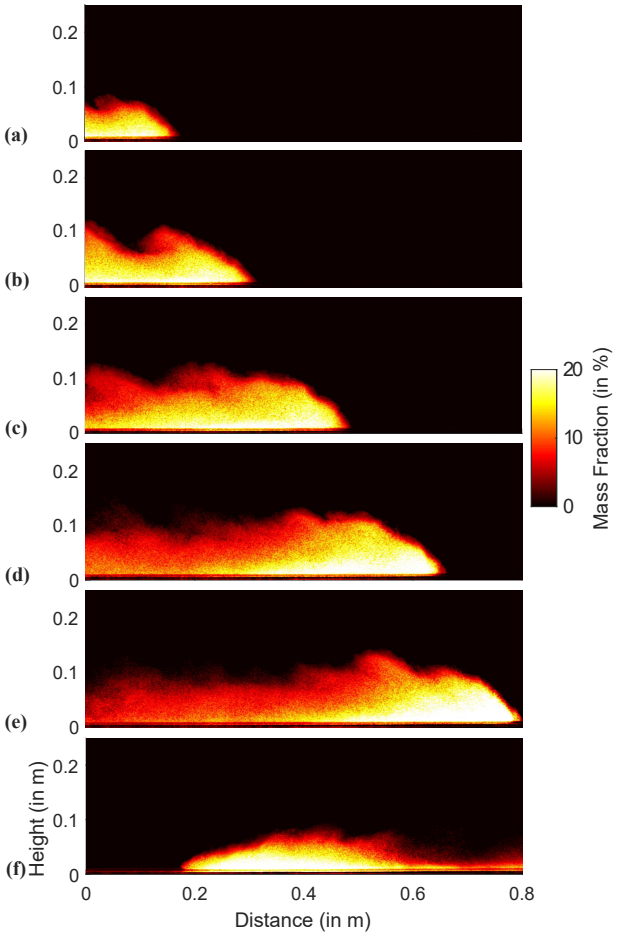

Fig. 7 Figure of a PLGC experiment with an initial density difference between the 2 compartments of $\Delta\rho = 24.4$ kg.m^{-3} and an initial mass fraction of $\Phi_m = 10.32\%$. These figures were obtained from photos taken (a) 4.25s, (b) 5.75s, (c) 7.25s, (d) 9.75s (e) 11.25s, (f) 33.25s after opening the gate.

current viscosity is limited and the nondimensional velocity number matches the theoretical value of 1/2.

For larger initial mass fractions concentrations ($\Phi_0 >$ 20%) the front velocity decreases quantitatively with Φ_0. This significant decrease occur when the effective viscosity departs strongly from the slowly varying linear behavior (11 a). In particular the front velocity has decreased by 25% with respect to the MGC in exp G. These results confirm the influence of particle concentration on the turbulent dynamics and the bulk velocity of dense PLGCs.

5 Conclusion

The dynamics of Particle Laden Gravity Currents has been investigated using high resolution light attenuation measurements, enabling to highlight two flow regimes.

In environmental and industrial applications, the carrier and surrounding fluids have different densities. Turbulent mixing processes at the interface between these two fluids control the current dynamics as previously discussed in dilute regimes (Sutherland et al. 2018). The presence of the particle impacts the turbulent dynamics of the flow via particle-fluid, particle-wall and particle-particle interactions. It also affects mixing between the carrier and surrounding fluids. Although the latter processes are not characterized in the present experiments, PILAT measurements indicate that the particle concentration, and hence the relative importance of turbulent mixing and effective viscous properties of the flow are heterogeneous in PLGCs. Very little is known about the impact of particle size on the dynamics of PLGCs in the turbulent regime at high concentrations.

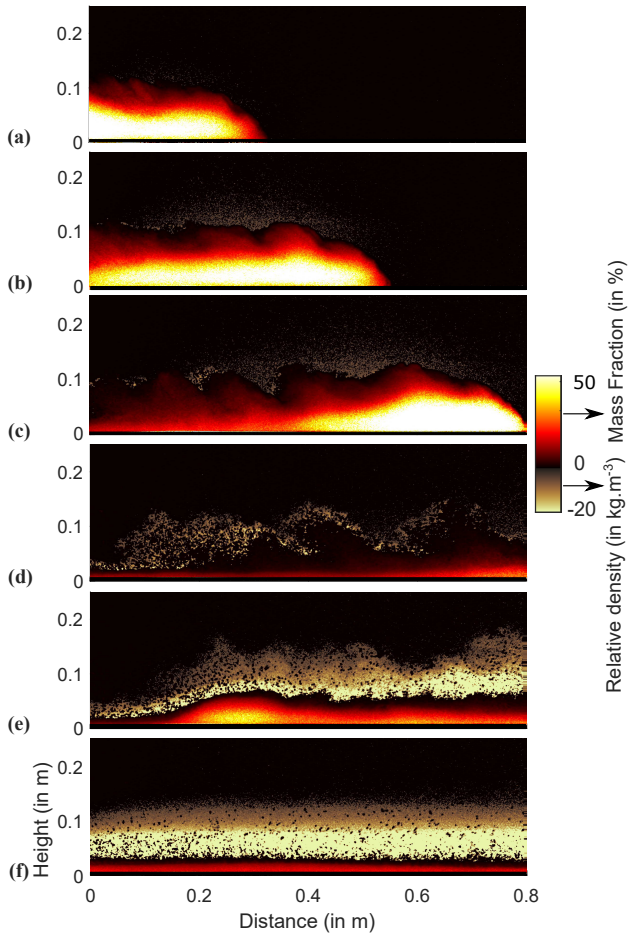

Fig. 8 Figure of a PLGC experiment with an initial density difference between the 2 compartments of $\Delta\rho = 24.4$ kg.m^{-3} and an initial mass fraction of $\Phi_m = 35\%$. Density exchange zones are visible and correspond to the values of the negative scale. These figures were obtained from photos taken (a) 5.25s, (b) 7.5s, (c) 9.5s, (d) 11.5s, (e) 13.5s, (f) 49.25s after opening the gate.

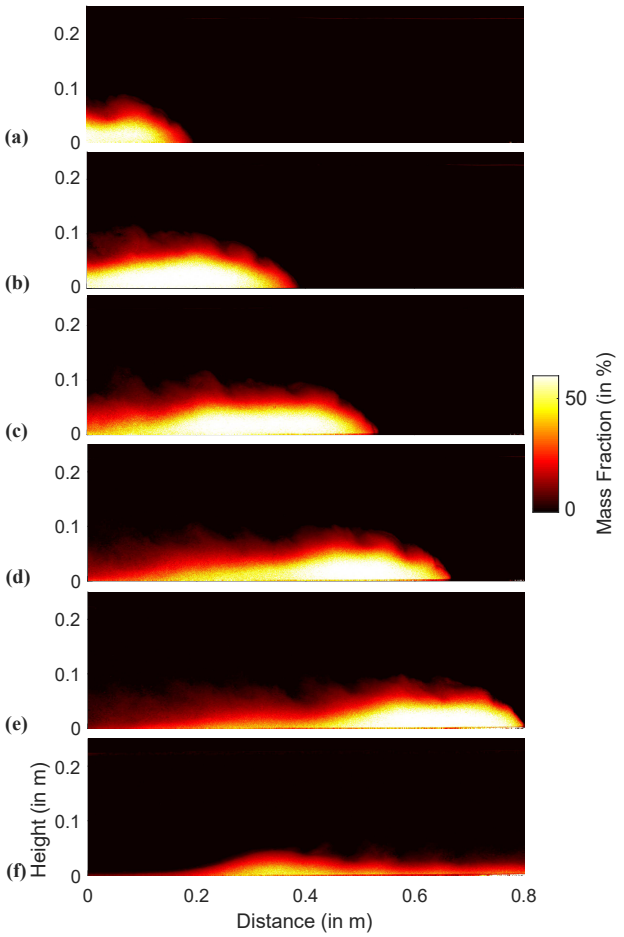

Fig. 9 Figure of a PLGC experiment with an initial density difference between the 2 compartments of $\Delta\rho = 24.4$ kg.m^{-3} and an initial mass fraction of $\Phi_m = 45\%$. These figures were obtained from photos taken (a) 5.25s, (b) 7.5s, (c) 9.5s, (d) 11.5s, (e) 13.5s, (f) 49.25s after opening the gate.

Recent experiments by Bougouin and Lacaze (2018) have highlighted four regime for granular collapse in a fluid with constant density. In future works, the combination of LAT/PILAT and PIV measurements in the surrounding fluid could enable to study the dynamics of this collapse for varying density of the carrier and surrounding fluids.

6 Declarations

6.1 Ethical Approval

not applicable

6.2 Competing interests

the authors have no competing interests as defined by Springer, or other interests that might be perceived to influence the results and/or discussion reported in this paper.

6.3 Authors' contributions

J.S. and Y.D. performed the experiments and wrote the main manuscript text.

O.F. ran the absorption/scattering model and wrote section 3.2.

M.R. performed preliminary experiments and analysis.

Y.D. and S.K. reviewed the manuscript.

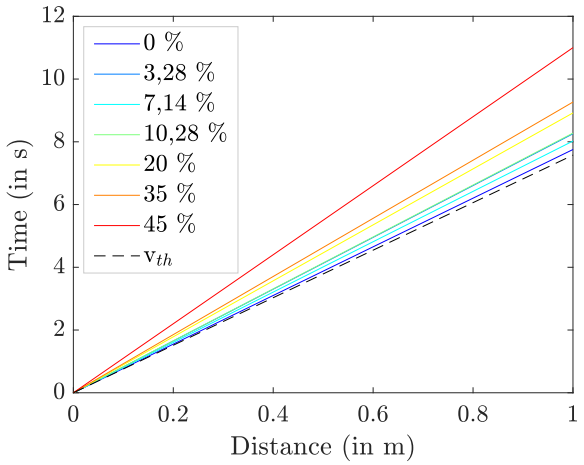

Fig. 10 Front position with respect to time for exp. A, B, C, D, E, F, G and the theoretical case.

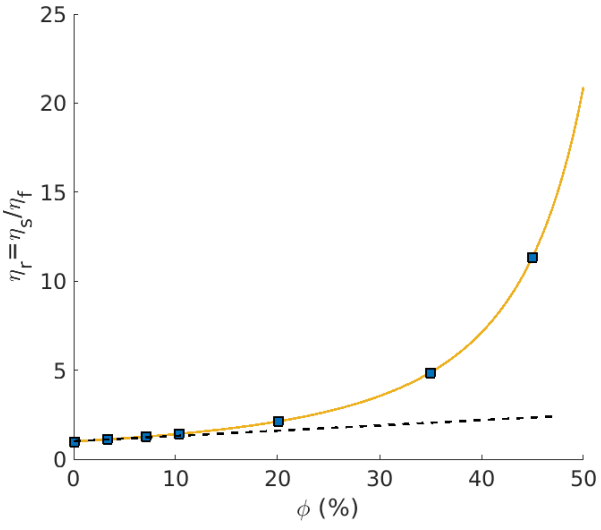

a)

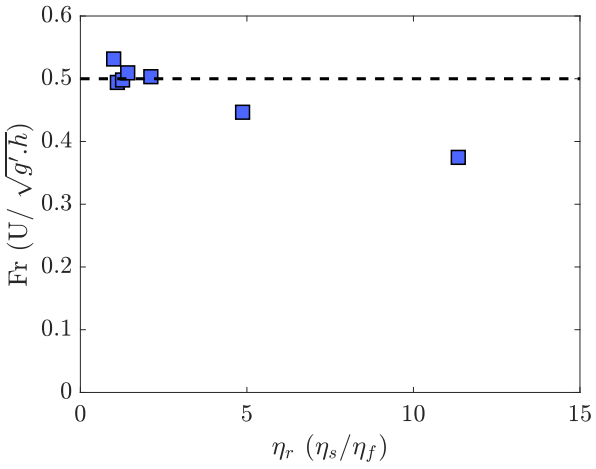

b)

Fig. 11 (a) Lock relative viscosity η_r expressed from Einstein's relation. The dashed line indicates the linear behavior at low concentration (b) Nondimensional front velocity as a function of relative viscosity η_r. The dashed line shows the prediction for a monophasic gravity current.

6.4 Funding

This work was funded by the research grant PALAGRAM granted by the French National Research Agency (ANR-19-CE30-0041).

6.5 Availability of data and materials

not applicable

References

Allgayer DM, Hunt GR (1991) On the application of the light-attenuation technique as a tool for non-intrusive buoyancy measurements. Experimental Thermal and Fluid Science 38:257–261

Balasubramanian S, Zhong Q (2018) Entrainment and mixing in lock-exchange gravity currents using simultaneous velocity-density measurements. Physics of Fluids 30:056601. doi:10.1063/1.5023033

Best JL, Kostaschuk RA, Peakall J, Villard PV, Franklin M (2005) Whole flow field dynamics and velocity pulsing within natural sediment-laden underflows. Geology 33(10):765–768. doi:10.1130/G21516.1. Publisher: GeoScienceWorld

Bonnecaze RT, Huppert HE, Lister JR (1993) Particle-driven gravity currents. Journal of Fluid Mechanics 250:339–369

Bougouin A, Lacaze L (2018) Granular collapse in a fluid: Different flow regimes for an initially dense-packing. Physical Review Fluids 3(6):064305. doi:10.1103/PhysRevFluids.3.064305. Publisher: American Physical Society

Cortés A, Rueda FJ, Wells MG (2014) Experimental observations of the splitting of a gravity current at a density step in a stratified water body. Journal of Geophysical Research: Oceans 119(2):1038–1053. doi:10.1002/2013JC009304. _eprint: https://onlinelibrary.wiley.com/doi/pdf/10.1002/2013JC009304

Cossu R, Forrest AL, Roop HA, Dunbar GB, Vandergoes MJ, Levy RH, Stumpner P, Schladow SG (2015) Seasonal variability in turbidity currents in lake ohau, new zealand, and their influence on sedimentation. Marine and Freshwater Research 67(11):1725–1739. doi:10.1071/MF15043. Publisher: CSIRO PUBLISHING

Davarpanah Jazi S, Wells MG (2020) Dynamics of settling-driven convection beneath a sediment-laden buoyant overflow: Implications for the length-scale of deposition in lakes and the coastal ocean. Sedimentology 67(1):699–720

Eberhart R, Kennedy J (1995) Particle swarm optimization. In: Proceedings of the IEEE international conference on neural networks. Citeseer, volume 4, 1942–1948

Fragoso A, Patterson M, JS W (2013) Mixing in gravity currents. Journal of Fluid Mechanics 734:R2

Galtier M, Blanco S, Caliot C, Coustet C, Dauchet J, El-Hafi M, Eymet V, Fournier RA, Gautrais J, Khuong A, Piaud B, Terrée G (2013) Integral formulation of null-collision Monte Carlo algorithms. Journal of Quantitative Spectroscopy and Radiative Transfer 125:57–68. doi:10.1016/j.jqsrt.2013.04.001

Hacker J, Linden PF, Dalziel SB (1996) Mixing in lock-release gravity currents. Dyn Atmos Oceans 24:183–195

Hitomi J, Nomura S, Murai Y, De Cesare G, Tasaka Y, Takeda Y, Park HJ, Sakaguchi H (2021) Measurement of the inner structure of turbidity currents by ultrasound velocity profiling. International Journal of Multiphase Flow 136:103540. doi:10.1016/j.ijmultiphaseflow.2020.103540

Howell JR, Mengüç MP, Daun K, Siegel R (2020) Thermal radiation heat transfer. CRC press

Hughes G, Linden PF (2016) Mixing efficiency in rundown gravity currents. Journal of Fluid Mechanics 809:691–704

Huppert HE (2006) Gravity currents: a personal perspective. Journal of Fluid Mechanics 554:299–322

Krug D, Holzner M, Lüthi B, Wolf M, Kinzelbach W, Tsinober A (2013) Experimental study of entrainment and interface dynamics in a gravity current. Experiments in Fluids 54(5):1530. doi:10.1007/s00348-013-1530-6

Maxworthy T, Leilich J, Simpson JE, Meiburg EH (2002) The propagation of a gravity current into a linearly stratified fluid. Journal of Fluid Mechanics 453:371–394. doi:10.1017/S0022112001007054

Micard D, Dossmann Y, Gostiaux L, Venaille A (2016) Mixing efficiency in a lock exchange experiment. In: VIIIth International Symposium on Stratified Flows. volume 1

Mountjoy JJ, Howarth JD, Orpin AR, Barnes PM, Bowden DA, Rowden AA, Schimel ACG, Holden C, Horgan HJ, Nodder SD, Patton JR, Lamarche G, Gerstenberger M, Micallef A, Pallentin A, Kane T (2018) Earthquakes drive large-scale submarine canyon development and sediment supply to deep-ocean basins. Science Advances 4(3):eaar3748. doi:10.1126/sciadv.aar3748. Publisher: American Association for the Advancement of Science Section: Research Article

Mulder T, Syvitski JPM, Migeon S, Faugères JC, Savoye B (2003) Marine hyperpycnal flows: initiation, behavior and related deposits. a review. Marine and Petroleum Geology 20(6):861–882. doi:10.1016/j.marpetgeo.2003.01.003

Negretti ME, Tucciarone FL, Wirth A (2021) Intruding gravity currents and re-circulation in a rotating frame: Laboratory experiments. Physics of Fluids 33(9):096607. doi:10.1063/5.0058629

Odier P, Chen J, Rivera MK, Ecke RE (2009) Fluid mixing in stratified gravity currents: the prandtl mixing length. Physical review letters 102(13):134504

Prastowo T, Griffiths R, Hughes G, Hogg AM (2008) Mixing efficiency in controlled exchange flows. Journal of Fluid Mechanics 600:235–244

Saha S, Salin D, Talon L (2013) Low reynolds number suspension gravity currents. The European Physical Journal E 36(8):85. doi:10.1140/epje/i2013-13085-0. Number: 8

Shahin A, Bachir W, Sayem El-Daher M (2019) Polystyrene microsphere optical properties by kubelka–munk and diffusion approximation with a single integrating sphere system: A comparative study. Journal of Spectroscopy 2019

Sher D, Woods AW (2015) Gravity currents: entrainment, stratification and self-similarity. Journal of Fluid Mechanics 784:130–162. doi:10.1017/jfm.2015.576. Publisher: Cambridge University Press

Shin JO, Dalziel SB, Linden PF (2004) Gravity currents produced by lock exchange. Journal of Fluid Mechanics 521:1–34. doi:10.1017/S002211200400165X. Publisher: Cambridge University Press

Simpson JE (1982) Gravity currents in the laboratory, atmosphere, and ocean. Annual Review of Fluid Mechanics 14(1):213–234. doi:10.1146/annurev.fl.14.010182.001241. _eprint: https://doi.org/10.1146/annurev.fl.14.010182.001241

Sutherland BR, Gingras MK, Knudson C, Steverango L, Surma C (2018) Particle-bearing currents in uniform density and two-layer fluids. Physical Review Fluids 3(2):023801. doi:10.1103/PhysRevFluids.3.023801. Number: 2

Sutherland BR, Lee B, Ansong JK (2012) Light attenuation experiments on double diffusive plumes and fountains. Physics of Fluids 24:066605

Tanimoto Y, Ouellette NT, Koseff JR (2021) Interaction between an inclined gravity current and a pycnocline in a two-layer stratification. Journal of Fluid Mechanics 887:A8. doi:10.1017/jfm.2020.9

Wells MG, Dorrell RM (2020) Turbulence processes within turbidity currents. Annual Review of Fluid Mechanics 53:59–83